

Limb-darkening and radii of M-type Mira models

K.-H. Hofmann¹, M. Scholz^{2,*}, and P.R. Wood³

¹ Max-Planck-Institut für Radioastronomie, Auf dem Hügel 69, D-53121 Bonn, Germany

² Institut für Theoretische Astrophysik der Universität Heidelberg, Tiergartenstrasse 15, D-69121 Heidelberg, Germany

³ Mount Stromlo and Siding Spring Observatories, Institute of Advanced Studies, The Australian National University, Weston Creek P.O. ACT 2611, Australia

Received 1 July 1998 / Accepted 2 September 1998

Abstract. Monochromatic limb-darkening and monochromatic radii predicted by the M-type Mira models of Bessell et al. (1996) and by new models described in Sect. 2 were computed for selected typical bandpasses used in interferometric and lunar occultation work. The new self-excited pulsation model series have periods and luminosities similar to *o* Ceti and R Leonis and comprise both fundamental ($1 M_{\odot}$, $1.2 M_{\odot}$) and first overtone ($2 M_{\odot}$) pulsators. Fundamental problems of defining and measuring radii of Mira variables caused by the large extension of their atmospheres are discussed. Effective temperatures defined in terms of Rosseland and continuum radii are generally well determinable with an inherent inaccuracy of a few percent, but special problems occur for very cool models or at phases when models are very cool, below about 2500 K.

Fits of simple uniform disk (UD), fully darkened disk (FDD) and Gauss-shaped limb-darkening curves to the model-predicted visibilities were performed and tabulated for a set of 26×12 model-filter-combinations covering a large variety of typical brightness distributions. These fits show that either the FDD or the Gauss curve is often a good or even excellent approximation. Limb-darkening curves for specific bandpasses of observational programs can be provided upon request.

Key words: techniques: interferometric – stars: AGB – stars: atmospheres – stars: late-type

1. Introduction

As Mira variables are among the largest stars, and as quite a few of them are located within a few hundred parsecs from the Sun, they are readily accessible to interferometric and lunar occultation techniques of radius measurement. Furthermore, their atmospheres are strongly extended configurations, so that observation of radii at wavelengths corresponding to absorption features of different strength (which are formed in different at-

mospheric layers) may be used as a tool to diagnose the atmospheric structure (e.g. Bessell et al. 1996 = BSW96). Though observational progress has been substantial in recent years, sound interpretation of observed data is still seriously hampered by insufficient knowledge of the limb-darkening of Miras. Present observational techniques are incapable of directly yielding the center-to-limb variation (CLV) of intensity over the stellar disk. Instead, observed interference patterns (from interferometry) or diffraction patterns (from lunar occultation) are used to derive angular sizes by comparison with patterns derived from model-predicted CLV shapes. Recent attempts at reconstructing empirical limb-darkening curves of Mira variables (R Leo: Di Giacomo et al. 1991; U Ori, Z Sgr, S Vir: Bogdanov & Cherepashchuk 1991; *o* Cet: Wilson et al. 1992) have been of rather limited success.

For non-Mira M giants, grids of models do exist and they have been used for predicting limb-darkening at various wavelengths (Manduca et al. 1977, Manduca 1979, Van Hamme 1993, Diaz-Cordoves et al. 1995, Claret et al. 1995, Hofmann & Scholz 1998 = HS98). However, modelling of the atmospheres of Mira variables is still in a rather primitive stage. Limb-darkening curves published by Scholz & Takeda (1987) are sometimes used by observers, although these are based on extremely simple Mira models by Bessell et al. (1989b) and cover only a small selection of stellar parameters and wavelengths. Unpublished limb-darkening predicted from the more elaborate BSW96 models has been used in a couple of recent observational Mira studies (e.g. Haniff et al. 1995, Weigelt et al. 1996). In this paper, we investigate CLV curves for Miras predicted at typical wavelengths that sample the large variation of monochromatic size of a Mira disk and are commonly chosen in observations. The Mira models used are those of BSW96, as well as some new models described in Sect. 2 and also used for analysis of spectral features (Scholz M., Wood P.R., in preparation).

The procedures we follow are essentially those adopted by HS98 for non-Mira M giants. We refer the reader to that paper and to the review of Scholz (1997) for a general discussion of problems related to limb-darkening and to radius determination using monochromatic light or light observed through filter bandpasses. We cannot present CLV curves for an extensive "grid"

Send offprint requests to: K.-H. Hofmann, (khh@speckle.mpifr-bonn.mpg.de)

* Visitor (March 1996) at Astrophysical Theory Centre (ATC), School of Mathematics and Mount Stromlo and Siding Spring Observatories, Australian National University

of M-type Mira models equivalent to the HS98 grid as no such grid exists for the large variety of Mira parameters (these include not only the stellar parameters but also different phases of different pulsation cycles). We rather present data for selected models which are expected to cover a wide range of the different CLV behaviors which occur in nature. In this way, observers can judge the reliability or uncertainty of derived angular sizes when a model-predicted or an artificial (e.g. uniform disk = UD, fully darkened disk = FDD, Gauss shape) limb-darkening is assumed.

2. Pulsation models

For our computations, we first create series of nonlinear pulsation models and we then take individual model density (and velocity) structures from these series and use them as input to a model atmosphere code with which non-grey temperature structures and CLV curves are constructed. Table 1 lists the Mira pulsation models from which the atmospheric structures were derived in terms of the "parent" star's parameters (mass M , luminosity L , Rosseland radius R_p referring to $\tau_{\text{Ross}} = 1$, mixing length to pressure scale height ratio l/H_p , effective temperature $T_{\text{eff}} \propto (L/R^2)^{1/4}$), the pulsation period P and the amplitudes of bolometric magnitude M_{bol} and pulsation velocity v . The first three model series (Z, D and E) are from BSW96. The remaining three model series (P, M and O) are new and will be described below.

The pulsation of the atmospheric outer layers of the models used by BSW96 was produced by applying a piston to the sub-atmospheric layers. The time variation of radius and luminosity at the piston was obtained from sequences of complete self-excited pulsation models that included all mass from the core ($r \sim 0.3R_\odot$) to the upper photosphere ($\tau_{\text{Ross}} \sim 0.001$). However, in the new models, the piston concept that only considers the behavior of the outer layers was abandoned and the atmospheric structures are taken directly from complete self-excited pulsation models. The pulsation code used was that described in BSW96 except that it has been updated to include the opacities produced by the OPAL group (Iglesias & Rogers 1993).

The new models were required to have a pulsation period of ~ 310 – 330 days, close to the periods of the well-studied nearby Miras α Ceti (332 days) and R Leo (310 days). As with the BSW96 models, two luminosities were considered: a value of $L \sim 6000L_\odot$ corresponding to the period-luminosity-relation for the LMC and a value of $L \sim 3500L_\odot$ suggested by a theoretical correction of the LMC P-L-relation to solar metallicity (cf. Wood 1990). Masses M of 1 to $2M_\odot$ were considered. At $M = 1$ and $1.2M_\odot$, it was not possible to get a stable pulsation with the higher luminosity value so that the lower luminosity value was used. At $M = 2M_\odot$, stable pulsation in the first overtone was possible with the high luminosity value (O series).

During model construction, a luminosity and mass were adopted and then the mixing length was adjusted to give the required period in the linear non-adiabatic pulsation code. The final parameter values for these non-pulsating "parent" models are given in Table 1.

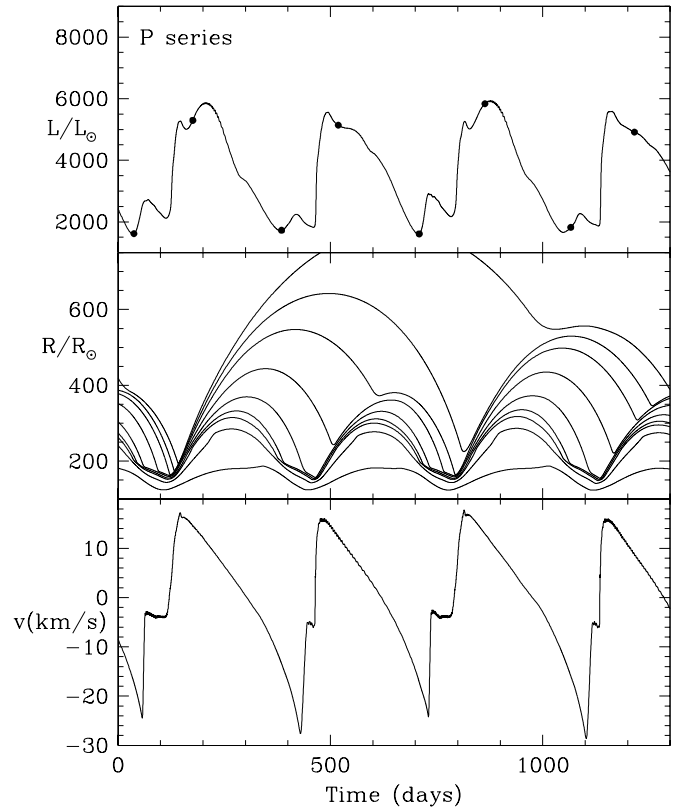


Fig. 1. Luminosity (top panel), radii of selected mass zones (middle panel) and the velocity of the 5th mass zone from the centre (bottom panel) plotted against time for P series models. The 5th zone from the centre corresponds roughly to the mean position over a pulsation cycle of Rosseland optical depth unity. In the top panel, the models selected for model atmosphere analysis are shown as solid circles.

Theoretical nonlinear pulsation models of Mira variables generally exhibit much larger amplitudes than are observed. This can be partly overcome by allowing the models to relax over a very large number of cycles (Wood 1995; Yaari & Tuchman 1995) and all the new model series were run through a long relaxation process. The new P series has essentially the same parameters as the BSW96 D series except that, with the new opacities and the relaxation technique, it was possible to obtain a stable limiting amplitude without introducing any non-physical damping via the α parameter used by BSW96. However, the P series does still have a larger bolometric amplitude (~ 1.3 mag, Table 1) than is typical for a Mira with $P \sim 330$ days (~ 1 mag, Feast et al. 1982).

In Figs. 1, 2 and 3, we show the time-dependence of L , radii of selected mass points, and the velocity of a mass point near Rosseland optical depth unity (averaged over a pulsation cycle). This velocity should be a good approximation to the velocity observed in Miras in the infrared (e.g. Hinkle et al. 1984). The models selected for detailed study in this paper are shown as filled circles on the luminosity curves in the figures. In general, the models were selected to be near maximum or minimum light. The complete selection of masses, luminosities, modes and phases of the BSW96 models and the present

Table 1. Properties of Mira model series (see text)

Series	Mode	$P(\text{days})$	M/M_\odot	L/L_\odot	R_p/R_\odot	l/H_p	T_{eff}	ΔM_{bol}	Δv
Z	f	334	1.0	6310	236	2.82	3370	1.0	36
D	f	330	1.0	3470	236	1.76	2900	1.0	31
E	o	328	1.0	6310	366	1.26	2700	0.7	15
P	f	332	1.0	3470	241	2.06	2860	1.3	40
M	f	332	1.2	3470	260	1.73	2750	1.2	42
O	o	320	2.0	5830	503	0.93	2250	0.5	22

Table 2. Properties of momentary Mira models (see text)

Model	ϕ_{vis}	L/L_\odot	R/R_p	R_T/R_p	$R_{1.04}/R_p$	$T_{\text{eff}}(R)$	$T_{\text{eff}}(R_T)$	$T_{\text{eff}}(R_{1.04})$
Z34890	1+0.0	7650	1.10	1.13	1.11	3350	3310	3340
Z35280	1+0.5	3860	0.89	0.90	0.89	3150	3130	3140
Z36180	2+0.0	7750	1.11	1.13	1.12	3350	3320	3340
Z36450	2+0.5	3830	0.89	0.90	0.89	3140	3120	3140
D27520	1+0.0	4490	1.04	1.07	1.04	3020	2980	3020
D27760	1+0.5	2210	0.91	0.93	0.90	2710	2680	2720
D28760	2+0.0	4560	1.04	1.08	1.05	3030	2980	3020
D28960	2+0.5	2170	0.91	0.94	0.90	2690	2650	2700
E8300	0+0.83	4790	1.16	1.47	1.07	2330	2070	2440
E8380	1+0.0	6750	1.09	1.12	1.09	2620	2590	2630
E8560	1+0.21	7650	1.17	1.22	1.15	2610	2560	2640
P71800	0+0.5	1650	1.20	1.51	0.90	2160	1930	2500
P73200	1+0.0	5300	1.03	1.06	1.04	3130	3080	3120
P73600	1+0.5	1600	1.49	1.83	0.85	1930	1740	2560
P74200	2+0.0	4960	1.04	1.06	1.04	3060	3040	3060
P74600	2+0.5	1680	1.17	1.46	0.91	2200	1970	2500
P75800	3+0.0	5840	1.13	1.19	1.14	3060	2990	3050
P76200	3+0.5	1760	1.13	1.64	0.81	2270	1880	2680
P77000	4+0.0	4820	1.17	1.21	1.16	2870	2820	2880
M96400	0+0.5	1470	0.93	1.20	0.84	2310	2030	2420
M97600	1+0.0	4910	1.19	1.28	1.18	2750	2660	2760
M97800	1+0.5	1720	0.88	1.15	0.83	2460	2150	2530
M98800	2+0.0	4550	1.23	1.35	1.20	2650	2530	2680
O64210	0+0.5	5020	1.12	1.24	1.00	2050	1950	2130
O64530	0+0.8	4180	0.93	0.96	0.91	2150	2120	2170
O64700	1+0.0	7070	1.05	1.09	1.01	2310	2260	2360

models should cover a good representative set of instantaneous Mira properties. The non-grey atmospheric temperature stratification of the new models was computed in the same way and with the same absorption and scattering coefficients (the therefrom derived Rosseland opacities and atmospheric τ_{Ross} scales match those used in the pulsation models in deep layers) as that of the BSW96 models so that predicted optical-depth radii, limb-darkening and spectral features can be compared directly. Since the atmospheres of the P and M models are substantially more extended and those of the O models are more compact than the atmospheres of the BSW96 models the model "surface" with zero incoming intensity was placed at $5 R_p$ (P and M series) and $2 R_p$ (O series) instead of $3 R_p$ as in BSW96. In Table 2, for each

of the new P, M and O model series, we give the approximate visual phase ϕ_{vis} , the instantaneous value of the luminosity L , the Rosseland radius R defined at $\tau_{\text{Ross}} = 1$, the temperature radius R_T at which the identity $L = 4\pi\sigma_{\text{SB}}R_T^2T^4$ holds (see Baschek et al. 1991; σ_{SB} = Stefan-Boltzmann radiation constant, T = local temperature at R_T), and the monochromatic radius $R_{1.04}$ defined at $\tau_{1.04} = 1$ in the $1.04 \mu\text{m}$ continuum window. The radii are given in units of the parent star's radii listed in Table 1. Also given in Table 2 are the effective temperatures $T_{\text{eff}}(R_x) \propto (L/R_x^2)^{1/4}$ corresponding to each of these radii. Those models of Table 3 of BSW96 which we consider in this paper are also entered for convenience.

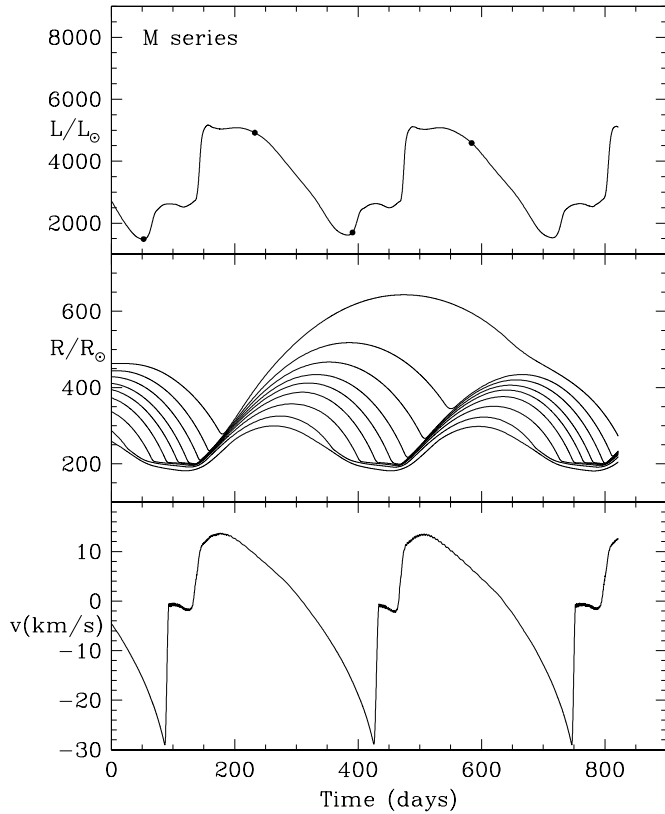


Fig. 2. Same as Fig. 1 but for M series models. The velocity in the bottom panel is for the 4th zone from the centre.

It is worth making a few comments on the complete set of model series. Firstly, in Table 1, note that the overtone models have large radii of $\sim 370\text{--}500 R_{\odot}$, more in agreement with recent observational estimates of Mira radii (eg. Haniff et al. 1995, van Belle et al. 1996) than the smaller radii ($R \sim 240 R_{\odot}$) of the fundamental mode pulsators. On the other hand, the pulsation velocity amplitudes of the overtone pulsators ($15\text{--}22 \text{ km s}^{-1}$) are far below the velocity amplitudes of $\sim 36 \text{ km s}^{-1}$ deduced (Wood 1987) from infrared observations (eg. Hinkle et al. 1984) of typical Miras variables. These inconsistencies mean that the identification of the mode of Mira variables remains a difficult problem. For this reason, we have included both fundamental and first overtone pulsators in this study (for a recent summary of the problem of mode determination in Miras, see Wood 1997). The P model series is followed over four successive cycles in order to demonstrate large cycle-to-cycle monochromatic radius differences (Sect. 5) also found in long-term observational series (e.g. Tuthill et al. 1995). Note also the sometimes striking deviations of the effective temperatures defined in terms of R_T or $R_{1.04}$ from the standard definition $T_{\text{eff}}(R)$ in cool models below about 2500 K. This consequence of flatter temperature and continuous optical depth gradients and of increased molecular band contamination of near-continuum “windows” at very low temperatures as well as limitations of these cool models will briefly be addressed in Sect. 4.

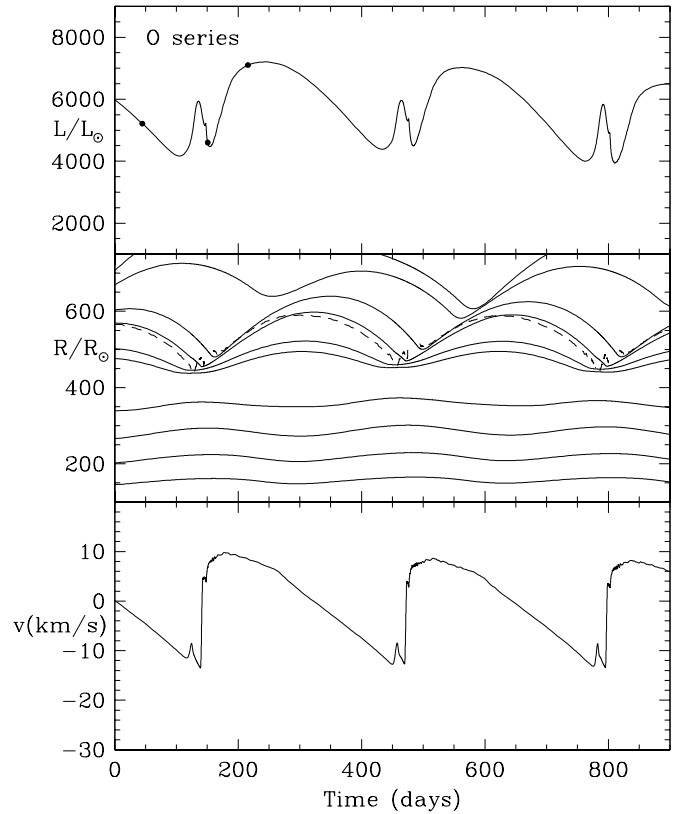


Fig. 3. Same as Fig. 1 but for O series models. The velocity in the bottom panel is for the 7th zone from the centre. The dashed line shows the position of Rosseland optical depth unity. The deep interior zones are shown in the middle panel so that the overtone nature of the pulsation can be readily seen.

3. Filters

We use the same set of broad-band and monochromatic (formal 1 nm full width) rectangular filters (Table 3) as HS98. These filters should represent the typical behavior of limb-darkening at continuum and near-continuum wavelengths as well as in TiO bands of different strengths relevant in interferometric and/or lunar occultation measurements. We offer to provide upon request CLV data for specific filters when these are needed for reduction of observational data of a star for which a suitable model is available.

Regarding “impure” filters assembling photons from both high-intensity and neighboring low-intensity spectral features originating from deep and high layers, respectively, we refer to the comments given in HS98. In particular we stress the problem of “leaking” filters meant to probe molecular bands but containing noticeable fractions of continuum photons from adjacent wavelengths. In the case of Mira atmospheres the problems arising from using such filters are even more severe because of very strong intensity contrasts and very large atmospheric extensions. The outermost portions of filter transmissions (or of instrumental profiles of interferometric spectrograms) must be very accurately determined for predicting reliable model CLV shapes. Moreover, in contrast to monochromatic limb-darkening

and monochromatic radii which may be a powerful tool for the diagnostics of the extended structure of the Mira atmosphere, limb-darkening of the stellar disk as seen through an "impure" filter and corresponding "filter radii" defined in terms of "averaged" photon formation layers contain little information about the stratification. The definition of the filter radius, R_{fil} , adopted here is that of Scholz & Takeda (1987).

4. Monochromatic limb-darkening and radii

A summary of basic problems of determining monochromatic radii of stars having an extended atmosphere was given in the HS98 model study of non-Mira M giants (see also Scholz 1997). We refer the reader to HS98 and only briefly recapitulate the essential points. (i) As M giant atmospheres are spherically extended, i.e. their geometrical thickness is not small compared to the star's total dimensions, any stellar radius has to be defined by picking out a specific atmospheric layer whose distance from the star's center one wants to call "radius". Numerous definitions may be found in the literature (Baschek et al. 1991). (ii) The conventional choice of "the" stellar radius also adopted in this paper (Sect. 2) is an optical-depth radius given in terms of unity Rosseland depth: $R = r(\tau_{\text{Ross}} = 1)$ (r = distance from the star's center). This Rosseland radius R then also serves for defining the effective temperature $T_{\text{eff}} \propto (L/R^2)^{1/4}$ and the "surface" gravity $g_s \propto M/R^2$ of the star. It is, however, only a convenient modelling parameter rather than a measurable quantity. (iii) Any observed radius-type quantity must depend on the wavelength of observation in an extended atmosphere since the observer sees higher layers in high-absorption spectral features than in low-absorption, e.g. near-continuum, features. In fact, the only directly observable quantity is the monochromatic center-to-limb variation (CLV) or limb-darkening of intensity from which a specific point in the outer portions of the monochromatic disk may be picked out for defining an intensity radius. For instance, the position of the CLV inflection point defines the photospheric intensity radii of the Sun at wavelengths λ which, of course, all coincide with each other (to within the limits of observational error) and also coincide with all optical-depth radii, $R_\lambda = r(\tau_\lambda = 1)$, because the solar photosphere is compact. (iv) Whilst an inflection-point or similar monochromatic intensity radius may be sensibly defined as well for most non-Mira and many Mira M giants at real-continuum wavelengths this conception fails in spectral regions where molecular band absorption produces extended outer wings or irregular shapes of the monochromatic limb-darkening curve. The choice of the specific point on the CLV to be called "radius" becomes rather arbitrary, and the position of the resulting intensity radius may be very different from that of the model-relevant optical-depth radius R_λ . (v) Since the limitations of presently available instrumentation does not allow reconstruction of the full CLV shape from the observed interference (interferometry) or diffraction (lunar occultation) pattern, CLV curves have to be taken for data reduction from model predictions, including the positions of any pre-chosen intensity radius point and of the R_λ optical-depth radius point on the CLV, and the angular scale of the disk

Table 3. Filters. Bandpasses are rectangular. Central wavelengths λ_c and full widths $\Delta\lambda$ are in μm .

Name	Feature	λ_c [μm]	$\Delta\lambda$ [μm]
0.40	continuum	0.405	0.01
0.58	near-continuum to moderate-TiO	0.5805	0.001
0.59	moderate-TiO to strong-TiO	0.5895	0.001
0.70	near-continuum to moderate-TiO	0.7015	0.001
0.71	moderate-TiO to strong-TiO	0.7100	0.001
0.75	near-continuum to moderate-TiO	0.7500	0.001
0.82	near-continuum	0.8185	0.001
0.92	near-continuum	0.9195	0.001
1.04	continuum	1.0465	0.001
1.63 H	continuum	1.633	0.30
2.20 K	continuum	2.195	0.40
3.80 L*	(impure) continuum	3.799	0.60

is the only adjustable parameter yielding the angular distance of this radius point from the disk's center.

There are three important points for which the fundamental problems of radius determination are here substantially exaggerated compared to the non-Mira case.

(1) Whilst the radius of an M giant measured at a continuum wavelength is very close to the Rosseland radius in non-Miras and in most Miras, noticeable deviations may be found in very cool Miras or at very cool Mira phases. This is a natural effect of the increasing influence of molecular band absorption upon the Rosseland extinction coefficient and of the flattening of $d\tau/dr$ gradients (cf. Bessell et al. 1989b, Scholz 1997). Furthermore, the problems of calculating physically meaningful Rosseland opacities with significant contribution from numerous lines with complex doppler shifts become so severe (e.g. Wehrse et al. 1992, Wehrse & Baschek 1998; Wehrse R., Baschek B., v. Waldenfels W., in preparation) that one should seriously consider replacing the Rosseland radius by a continuum radius as reference modelling radius in very late-type Mira work. The assignment of a quantity to be called the Mira's "effective temperature" becomes rather arbitrary under these circumstances. The Rosseland radius R given here and its associated T_{eff} value, which are based upon very simple line treatment (cf. Bessell et al. 1989a, b, 1991), should be considered as guiding quantities only below, say, 2500 K. A similarly adverse situation occurs with respect to the so-called temperature radius R_T (see Sect. 2) which is not based on the arbitrary choice of a specific distance r from the star's center but becomes very dependent on model details in cool stars with flat dT/dr gradients. The numerical examples of three different radii and corresponding effective temperature entered in Table 2 illustrate these problems. Note

also that dust formation and dust absorption is not included in our equation of state and in our opacities, respectively. If dust particles occur in the outermost layers of very cool Mira atmospheres they may noticeably affect the temperature structure and infrared limb-darkening.

(2) The behavior of continuous and Rosseland extinction coefficients as well as the increased strength of molecular bands and the increased extension of the atmosphere of a Mira compared to a non-Mira giant makes the "scaling" procedure for converting a measured radius-type quantity into a model-relevant optical-depth radius (see the detailed discussion in Sect. 4 of HS98) more delicate and more model dependent. In addition, the interpretation of, and physically meaningful derivation of pertinent filter radii from, Mira observations in "impure" filters assembling photons from both high-intensity and low-intensity spectral features originating from deep and high layers, respectively, is more difficult than in the non-Mira case.

(3) Scholz & Takeda (1987) noticed for the first time in their limb-darkening study of the simple Bessell et al. (1989b) Mira models that extended wing-like features occur in the outer portions of various monochromatic center-to-limb variations. More elaborated models since have confirmed this phenomenon, and recent interferometric observations at relevant wavelengths reaching sufficient accuracies in the near-minimum visibility domain indicate that a "Gauss-type" CLV sometimes yields a better fit of data than conventional CLV curves having a steep decline towards the "edge" of the monochromatic disk (e.g. Tuthill et al. 1994, Haniff et al. 1995, R Leo data in preparation). In fact, the BSW96 and our new Mira models predict the occurrence of a wide range of wing-like CLV features ranging from low-level intensity plateaus to almost perfect Gauss shapes of some limb-darkening curves (e.g. Fig. 2 of Scholz 1997). CLV shapes with small Gauss-like wings also occur in non-Miras occasionally (Watanabe & Kodaira 1979, Scholz & Takeda 1987, HS98) but are much less conspicuous than in Miras. Hestroffer (1997) has suggested a very flexible parametrization of this type of limb-darkening covering a large variety of different shapes in terms of one parameter α (see Fig. 1 of Hestroffer's paper). Whether or not wing-like features and even extreme Gauss curves form depends essentially on the temperature-dependence of the Planck function and on the intensity contribution function (Scholz 1997) in the relevant layers at the considered wavelength. Unfortunately, interferometric observers merely see the inner high-intensity zones of the monochromatic disk in such cases whereas the position of the "radius", e.g. the $\tau_\lambda = 1$ optical-depth radius, is located somewhere in the outer low-intensity zones. This illuminates the fundamental dilemma of any indirect radius measurement whether through interferometry or through lunar occultation: observed data are dominated by the appearance of the brightest parts of the stellar disk which may or may not be closely related to a radius-type quantity. Only when very high accuracies are obtained beyond the central portion of the 1st maximum of the visibility will contributions from the dim outer disk zones begin to show up in interferometric data. This means that one depends very sensitively upon a

reliably model-predicted limb-darkening curve for extracting a radius from these data.

Wing-like features preferentially occur when noticeable molecular band absorption affects the CLV. In a recent study of the Mira-like variable R Dor, Jacob A.P., Bedding T.R., Robertson J.G. & Scholz M. (= JBRS, in preparation) point out that in the most extreme cases of strong near-infrared TiO bands it may even happen that the CLV has a relatively narrow bright core that dominates the central visibility maximum in such a way that it appears broader than visibilities belonging to adjacent wavelengths of weaker TiO absorption. Thus, the disk's size seems to be smaller at first glance in the light of the strongest bands contrary to the physical expectation, and only the knowledge of the complete CLV including its extended outer portion reveals the true large size of the strong-TiO monochromatic disk. Tests show (JBRS) that the width of this bright core increases quickly as the temperature gradient in the uppermost model layers that governs the behavior of Planck functions and intensity contribution functions is flattened artificially, which means that the CLV input of data reduction is unpleasantly sensitive to subtle details of the upper model structure. This is a really severe problem because the most strongly saturated molecular bands are most strongly affected by flaws of the here adopted opacity approximations (Bessell et al. 1989 a, b, 1991; BSW96) and because the near-surface layers where the very strong bands are formed have, in the coolest models, temperatures below the 750 K limit beyond which our equation of state and opacities become more and more unrealistic (a 750 K temperature cutoff was therefore chosen for computation of spectral features in the new model series). It is in fact not clear at the present whether or not such extreme cases of limb-darkening do occur in nature. More details are discussed in the study of JBRS. Numerical examples are presented in Sect. 5. Note also in this context that the full half-width of an adopted Gauss CLV used in this and in observational papers measures the compactness of the brightness distribution on the disk, but it does not measure and is not directly related to R_λ or similar radius-type quantities.

5. Limb-darkening shapes and visibility fits

Table 4a/4b gives wavelength-dependent model radii for our filter selection of Table 3 as well as radii resulting from fitting visibilities calculated from model limb-darkening curves by means of artificial (UD, FDD, Gauss shape) limb-darkening curves. This table is the counterpart to Table 2 of HS98 and we refer to HS98 for a detailed description of the visibility fitting procedure.

The first line of each model-filter entry in Table 4a/4b gives the value of the filter radius R_{fil} according to the definition of Scholz & Takeda (1987) which equals the monochromatic optical-depth radius $R_\lambda = r(\tau_\lambda = 1)$ in the limiting case of a strictly monochromatic filter. It also gives in parentheses the position R_{10} on the disk where the intensity reaches the level corresponding to 10% of the center value. Both radii are here given in units of the phase-independent parent star radius R_p in contrast to Table 2 of HSW98 where the reference radius is R

Table 4a. Monochromatic radii in selected filters. First line: filter designations after Table 3. Following upper lines: model designation after Table 2 and R_{fil}/R_p (R_{10}/R_p) ratios (see text). Following lower lines: UD, FDD and Gauss radii in units of R_{fil} obtained by fitting the central maximum of the model clv visibility by means of a UD, FDD and Gauss clv, plus accuracy value (average deviation between the *true* limb-darkening and the fitted artificial clv in the space domain in % of the central intensity of the *true* limb-darkening; see HS98). Continued on Table 4b.

Filter Model	0.40	0.58	0.59	0.70	0.71	0.75	0.82	0.92	1.04	1.63 H	2.20 K	3.80 L*
Z34890	1.13 (1.19) 0.89/13 0.99/5 0.61/10	1.27 (1.14) 0.72/15 0.80/7 0.50/6	1.45 (1.18) 0.67/15 0.75/8 0.46/4	1.17 (1.19) 0.84/13 0.93/5 0.58/10	2.04 (1.63) 0.63/18 0.70/11 0.43/1	1.12 (1.15) 0.90/11 1.00/3 0.62/14	1.12 (1.16) 0.92/10 1.03/2 0.64/16	1.12 (1.16) 0.94/9 1.05/3 0.65/18	1.11 (1.18) 0.94/9 1.05/2 0.65/18	1.08 (1.13) 0.95/9 1.06/3 0.66/19	1.08 (1.09) 0.96/7 1.07/6 0.66/22	1.09 (1.14) 0.98/5 1.09/7 0.68/23
Z35280	0.90 (0.93) 0.90/13 1.00/6 0.62/9	1.72 (1.74) 0.83/15 0.93/6 0.57/8	2.11 (1.69) 0.66/16 0.73/7 0.45/7	1.50 (1.68) 0.88/18 0.98/12 0.61/4	2.36 (1.91) 0.66/17 0.73/8 0.46/6	1.29 (0.96) 0.67/18 0.75/12 0.46/5	0.90 (0.91) 0.95/15 1.06/8 0.65/9	0.90 (0.91) 0.97/12 1.08/7 0.66/13	0.89 (0.88) 0.94/8 1.04/5 0.65/20	0.88 (0.88) 0.95/9 1.05/5 0.65/17	0.88 (0.89) 1.03/14 1.15/10 0.70/16	0.88 (0.89) 1.16/20 1.29/14 0.79/15
Z36180	1.14 (1.25) 0.89/14 0.99/5 0.61/9	1.30 (1.10) 0.70/15 0.78/7 0.48/6	1.84 (1.21) 0.53/16 0.59/9 0.37/2	1.18 (1.20) 0.84/14 0.93/6 0.58/9	2.66 (1.68) 0.52/19 0.58/13 0.35/2	1.13 (1.15) 0.89/11 1.00/3 0.62/14	1.12 (1.22) 0.92/10 1.03/2 0.64/15	1.12 (1.23) 0.94/9 1.05/3 0.65/17	1.12 (1.17) 0.94/10 1.05/2 0.65/18	1.08 (1.13) 0.95/9 1.06/3 0.66/19	1.08 (1.08) 0.96/7 1.07/5 0.66/22	1.09 (1.14) 0.98/5 1.09/7 0.67/23
Z36450	0.90 (0.97) 0.90/13 1.00/6 0.62/9	1.75 (1.74) 0.83/15 0.92/6 0.57/8	2.16 (1.72) 0.65/16 0.73/7 0.45/7	1.52 (1.73) 0.91/18 1.01/11 0.62/3	2.30 (1.98) 0.70/17 0.78/8 0.48/7	1.34 (0.97) 0.67/20 0.75/13 0.46/5	0.90 (0.93) 0.95/15 1.06/9 0.66/8	0.90 (0.93) 0.97/12 1.08/7 0.67/12	0.89 (0.88) 0.94/8 1.04/5 0.65/20	0.88 (0.88) 0.95/9 1.05/5 0.65/17	0.88 (0.89) 1.04/15 1.15/10 0.71/15	0.88 (0.89) 1.17/21 1.31/14 0.81/14
D27520	1.06 (1.12) 0.88/13 0.98/4 0.61/11	1.22 (1.21) 0.87/11 0.98/1 0.61/16	1.27 (1.16) 0.78/12 0.87/3 0.54/12	1.19 (1.20) 0.90/11 1.00/1 0.62/16	2.06 (1.15) 0.46/16 0.82/14 0.32/4	1.14 (1.15) 0.82/14 0.91/5 0.56/9	1.08 (1.15) 0.87/12 0.92/10 0.60/12	1.06 (1.11) 0.91/11 1.02/3 0.63/15	1.04 (1.12) 0.94/9 1.05/3 0.65/19	1.02 (1.07) 0.94/9 1.04/3 0.64/18	1.02 (1.07) 0.95/7 1.06/5 0.66/19	1.03 (1.14) 0.99/7 1.10/5 0.68/21
D27760	0.91 (0.92) 0.89/12 0.99/2 0.62/13	1.37 (1.35) 0.81/14 0.90/5 0.56/9	1.71 (1.36) 0.63/15 1.05/6 0.44/6	1.18 (1.38) 0.94/15 1.05/6 0.65/8	1.84 (1.58) 0.70/15 0.78/7 0.48/7	1.08 (1.21) 0.86/17 0.96/9 0.60/4	0.95 (1.06) 0.92/13 1.02/6 0.63/9	0.92 (0.96) 0.91/11 1.02/4 0.63/13	0.90 (0.91) 0.94/8 1.04/4 0.65/20	0.89 (0.89) 0.94/10 0.95/19 0.65/15	0.89 (0.93) 1.00/13 1.11/7 0.69/13	0.89 (1.33) 1.11/16 1.24/10 0.76/12
D28760	1.06 (1.11) 0.88/13 0.98/4 0.61/11	1.23 (1.24) 0.89/11 0.99/1 0.62/16	1.27 (1.24) 0.86/11 1.01/1 0.59/16	1.20 (1.25) 0.90/11 1.01/1 0.62/15	1.30 (1.20) 0.81/12 0.92/14 0.56/13	1.15 (1.14) 0.82/14 0.91/5 0.57/9	1.09 (1.14) 0.87/12 1.02/3 0.60/12	1.06 (1.16) 0.91/11 1.02/3 0.63/15	1.05 (1.12) 0.94/9 1.05/3 0.65/19	1.03 (1.12) 0.94/9 1.05/3 0.65/18	1.03 (1.12) 0.96/7 1.07/5 0.66/20	1.03 (1.19) 0.99/8 1.10/5 0.68/21
D28960	0.91 (0.96) 0.89/12 1.00/3 0.62/12	1.39 (1.32) 0.80/14 0.89/5 0.55/9	1.80 (1.34) 0.59/15 1.04/6 0.41/5	1.19 (1.40) 0.93/14 1.04/6 0.65/9	2.07 (1.62) 0.63/16 0.70/8 0.43/5	1.11 (1.22) 0.88/17 0.97/9 0.60/4	0.96 (1.08) 0.92/14 1.03/6 0.64/9	0.94 (1.00) 0.91/12 1.02/4 0.63/12	0.90 (0.96) 0.94/11 1.05/3 0.65/19	0.90 (0.93) 0.94/11 1.05/4 0.65/14	0.91 (0.96) 1.00/13 1.11/7 0.69/12	0.90 (1.32) 1.12/17 1.24/9 0.77/11
E8300	1.09 (1.30) 0.96/15 1.07/7 0.66/8	1.62 (1.54) 0.79/13 0.88/4 0.55/12	1.72 (1.38) 0.67/14 0.75/6 0.46/8	1.55 (1.52) 0.87/12 0.97/2 0.60/15	2.06 (1.43) 0.57/15 0.63/8 0.39/5	1.55 (1.53) 0.85/13 0.95/3 0.59/12	1.39 (1.53) 0.94/13 1.04/4 0.65/13	1.30 (1.55) 0.97/13 1.08/5 0.67/11	1.06 (1.26) 0.99/12 1.10/5 0.68/15	1.12 (1.45) 1.00/17 1.12/9 0.69/7	1.14 (1.55) 1.18/16 1.20/10 0.75/6	1.16 (1.62) 1.18/16 1.32/7 0.81/9
E8380	1.10 (1.20) 0.92/13 1.03/5 0.64/9	1.66 (1.61) 0.82/13 0.92/3 0.57/13	1.83 (1.51) 0.67/15 0.75/6 0.46/8	1.56 (1.70) 0.91/12 1.01/3 0.63/14	2.29 (1.54) 0.55/16 0.61/8 0.38/5	1.52 (1.61) 0.87/15 0.97/6 0.60/9	1.32 (1.54) 0.95/16 1.05/7 0.68/7	1.18 (1.49) 0.98/16 1.10/8 0.68/7	1.08 (1.15) 0.95/9 1.06/4 0.65/18	1.07 (1.19) 0.98/13 1.09/7 0.67/12	1.10 (1.56) 1.19/16 1.14/9 0.71/10	1.08 (1.69) 1.19/19 1.32/11 0.81/9
E8560	1.17 (1.20) 0.89/12 0.99/3 0.61/12	1.68 (1.64) 0.83/14 0.92/4 0.57/11	1.97 (1.56) 0.65/15 0.73/7 0.45/7	1.51 (1.69) 0.94/14 1.04/4 0.65/12	2.38 (1.74) 0.58/16 0.64/8 0.40/5	1.45 (1.66) 0.89/17 0.99/9 0.61/6	1.24 (1.47) 0.94/14 1.05/7 0.65/9	1.22 (1.33) 0.91/12 1.02/5 0.64/11	1.15 (1.20) 0.95/12 1.05/2 0.65/18	1.13 (1.19) 0.94/10 1.06/4 0.65/13	1.14 (1.32) 1.00/13 1.12/7 0.69/12	1.13 (1.62) 1.12/16 1.24/9 0.76/11

(see Table 2 for phase-dependent R/R_p ratios). R_{10} contains some rough information about the occurrence of wing-like outer portions of the CLV curve. Close agreement of both numbers usually means that the brightness disk has a rather sharp edge whose position is a good approximation to the filter radius. We also find, however, numerous pairs of numbers which differ by more than just a few percent, in particular for very cool and very extended models. We recall that, in principle, any CLV has an extended wing because there are at any wavelength more or less tiny light contributions from the outer low-density layers of the star's atmosphere. If the center-to-limb brightness contrast is relatively low owing to relevant Planck contributions these wings may show up clearly although these layers do not strongly contribute to the $\tau_\lambda = -\int_{\text{surface}}^r k_\lambda(r) \times \rho(r) dr$ integration ($k_\lambda =$ extinction coefficient per mass unit; $\rho =$ density) yielding $\tau_\lambda = 1$ at $r = R_\lambda$ in the monochromatic limit. In such cases, the 10% level is positioned noticeably outside R_λ , and the R_λ radius is usually close to the steeper-gradient inner portions of the limb-darkening curve so that interferometric or lunar occultation data can be interpreted with due caution without detailed knowledge of the outermost CLV shape. Typical examples are the H and K filters which exhibit CLV wings in several of our models despite little molecular band contamination. In the opposite extreme, the center-to-limb contrast is so high that the wings are hardly

seen when the intensity is measured in units of its center value, but the outermost dim layers contribute substantially to the τ_λ integration. This behavior is typically found in the light of strong molecular bands whose limb-darkening curve is in the most extreme cases Gauss-like, with R_λ positioned at a near-zero-intensity level far outside R_{10} . We here repeat, however, our warning of the preceding section: these extreme CLV shapes strongly depend upon details of opacities and of the structure of the outermost model layers and may readily change when slightly different model parameters or modelling assumptions are adopted.

The numbers in Table 4a/4b below the R_{fil} (R_{10}) line are UD, FDD and Gauss radii in units of R_{fil} obtained by fitting the central maximum of the model-predicted CLV by means of an artificial UD, FDD and Gauss CLV, respectively. The attached accuracy value is the average deviation between the model-predicted ("true") CLV and the fitted artificial CLV in the space domain in % of the central intensity of the model-predicted CLV. Deviations of 0 to 4% (4 to 12%; more than 12%) indicate good (fair; poor) fits. We refer to HS98 for details. The HS98 study shows that FDD limb-darkening is a good or fair approximation to model-predicted limb-darkening for almost any model-filter combination in the case of non-Mira M giants. The numbers in Table 4a/4b show that this is still true

Table 4b.

Filter Model	0.40	0.58	0.59	0.70	0.71	0.75	0.82	0.92	1.04	1.63 H	2.20 K	3.80 L*
P71800	0.99 (1.21)	1.56 (1.46)	2.04 (1.29)	1.52 (1.46)	2.52 (1.68)	1.52 (1.47)	1.35 (1.46)	1.23 (1.49)	0.90 (1.17)	1.02 (1.48)	1.04 (1.54)	1.14 (1.50)
	0.98/16	0.77/13	0.51/15	0.85/12	0.58/17	0.83/13	0.93/13	0.99/14	1.07/14	1.09/19	1.19/18	1.19/14
	1.10/8	0.86/4	0.57/7	0.94/2	0.64/10	0.92/3	1.03/4	1.10/5	1.19/6	1.21/11	1.32/10	1.33/6
	0.68/6	0.53/11	0.35/5	0.59/14	0.39/2	0.57/12	0.64/12	0.68/9	0.74/11	0.74/4	0.81/5	0.83/10
P73200	1.06 (1.11)	1.31 (1.30)	2.38 (1.50)	1.22 (1.25)	3.59 (1.83)	1.11 (1.07)	1.06 (1.11)	1.05 (1.16)	1.04 (1.08)	0.99 (1.06)	0.99 (1.07)	1.01 (1.10)
	0.90/13	0.83/15	0.50/16	0.85/14	0.42/17	0.81/13	0.89/12	0.93/10	0.94/9	0.95/10	0.97/8	1.00/7
	1.00/4	0.57/7	0.56/9	0.95/6	0.47/10	0.91/5	1.00/3	1.04/3	1.05/3	1.06/2	1.09/4	1.12/6
	0.62/11	0.57/6	0.34/3	0.59/7	0.29/1	0.56/10	0.62/13	0.64/16	0.65/19	0.66/17	0.67/18	0.69/20
P73600	0.95 (1.21)	2.26 (1.78)	3.12 (2.14)	1.87 (1.78)	1.90 (1.77)	1.48 (1.70)	1.29 (1.63)	0.85 (1.19)	1.04 (1.60)	1.12 (1.88)	1.30 (2.11)	
	1.02/17	0.64/15	0.55/16	0.77/14	0.77/15	0.93/15	1.00/15	1.11/16	1.21/21	1.36/19	1.36/15	
	1.13/10	0.72/8	0.62/8	0.86/6	1.03/7	1.12/7	1.23/8	1.35/15	1.52/13	1.52/13	1.52/13	
	0.70/2	0.44/5	0.38/3	0.53/8	0.53/6	0.64/7	0.70/5	0.76/9	0.83/8	0.94/7	0.94/5	
P74200	1.05 (1.03)	2.89 (2.50)	3.93 (2.74)	2.27 (2.55)	4.35 (3.46)	2.23 (1.28)	1.07 (1.03)	1.05 (1.04)	1.04 (1.04)	1.03 (1.04)	1.11 (1.03)	1.03 (2.54)
	0.88/13	0.71/15	0.55/16	0.90/16	0.65/18	0.64/22	1.00/19	0.99/15	0.93/8	1.02/15	1.26/25	1.86/26
	0.98/4	0.80/8	0.61/9	1.00/10	0.72/9	0.71/17	1.11/12	1.09/9	1.04/4	1.13/10	1.40/18	2.06/21
	0.60/11	0.49/6	0.38/4	0.62/3	0.44/5	0.43/13	0.68/7	0.67/11	0.65/20	0.68/13	0.86/13	1.28/17
P74600	0.99 (1.22)	1.50 (1.38)	2.02 (1.28)	1.47 (1.44)	2.44 (1.69)	1.46 (1.45)	1.33 (1.44)	1.21 (1.39)	0.91 (1.18)	1.00 (1.42)	1.02 (1.45)	1.10 (1.56)
	0.97/15	0.77/13	0.52/15	0.85/11	0.57/16	0.83/12	0.92/13	0.98/14	1.06/14	1.07/19	1.16/18	1.19/14
	1.08/7	0.85/4	0.58/8	0.95/1	0.64/9	0.93/3	1.03/3	1.09/5	1.18/6	1.19/11	1.30/10	1.33/6
	0.67/6	0.53/11	0.36/4	0.59/15	0.39/3	0.57/13	0.64/13	0.67/10	0.73/11	0.74/4	0.81/5	0.83/9
P75800	1.18 (1.26)	1.60 (1.51)	3.65 (1.81)	1.37 (1.41)	4.60 (3.12)	1.33 (1.27)	1.22 (1.26)	1.17 (1.35)	1.14 (1.23)	1.07 (1.23)	1.06 (1.19)	1.09 (1.30)
	0.90/13	0.79/16	0.41/17	0.91/13	0.54/19	0.77/15	0.93/12	0.97/12	0.96/10	0.97/12	1.01/11	1.07/12
	1.01/4	0.88/9	0.46/11	1.02/6	0.60/11	0.86/7	0.97/5	1.04/4	1.06/2	1.08/3	1.12/5	1.19/6
	0.62/10	0.54/6	0.28/1	0.63/10	0.37/1	0.54/7	0.60/11	0.64/14	0.66/17	0.66/13	0.69/14	0.73/15
P76200	0.83 (1.09)	1.95 (1.67)	2.30 (1.79)	1.69 (1.69)	2.64 (1.94)	1.71 (1.67)	1.36 (1.62)	1.19 (1.49)	0.81 (1.06)	0.93 (1.40)	0.96 (1.71)	1.00 (1.88)
	1.05/18	0.70/15	0.62/15	0.82/13	0.64/16	0.80/14	0.95/15	1.00/17	1.04/14	1.15/22	1.38/21	1.57/17
	1.17/10	0.78/7	0.69/7	0.92/5	0.71/9	0.89/6	1.06/7	1.11/10	1.16/8	1.28/15	1.54/15	1.75/10
	0.72/3	0.48/7	0.43/5	0.57/10	0.43/4	0.55/7	0.66/5	0.69/2	0.72/12	0.79/8	0.95/9	1.07/7
P77000	1.19 (1.16)	2.00 (1.97)	2.47 (1.81)	1.79 (2.03)	3.43 (1.94)	1.64 (1.77)	1.23 (1.41)	1.21 (1.21)	1.16 (1.18)	1.13 (1.16)	1.14 (1.21)	1.13 (1.94)
	0.88/13	0.84/12	0.60/14	0.94/14	0.46/17	0.83/19	0.95/16	0.93/12	0.94/9	0.96/11	1.04/15	1.18/19
	0.98/3	0.93/3	0.67/6	1.04/5	0.51/9	0.92/13	1.05/9	1.03/6	1.05/3	1.07/5	1.15/9	1.31/12
	0.61/12	0.58/12	0.41/8	0.64/9	0.32/2	0.56/4	0.65/6	0.64/11	0.65/19	0.66/14	0.71/12	0.81/11
M96400	0.86 (1.00)	1.43 (1.27)	1.71 (1.33)	1.28 (1.27)	1.82 (1.49)	1.29 (1.26)	1.09 (1.23)	0.99 (1.17)	0.84 (0.98)	0.90 (1.20)	0.92 (1.33)	0.94 (1.39)
	0.94/13	0.72/14	0.61/15	0.84/12	0.66/15	0.81/14	0.94/14	0.98/15	0.97/9	1.01/17	1.13/18	1.25/16
	1.04/5	0.81/6	0.69/7	0.94/4	0.73/7	0.91/5	1.04/5	1.09/6	1.08/4	1.12/10	1.26/10	1.39/7
	0.65/10	0.50/8	0.43/5	0.58/12	0.45/6	0.56/9	0.65/9	0.67/8	0.67/17	0.70/6	0.78/5	0.86/7
M97600	1.23 (1.35)	1.51 (1.48)	1.94 (1.37)	1.46 (1.50)	2.57 (1.63)	1.41 (1.48)	1.34 (1.43)	1.29 (1.42)	1.18 (1.30)	1.15 (1.31)	1.15 (1.43)	1.15 (1.48)
	0.92/13	0.86/12	0.59/14	0.91/10	0.51/16	0.88/12	0.90/12	0.91/13	0.96/10	0.96/12	0.99/13	1.07/13
	1.02/4	0.96/2	0.65/6	1.02/2	0.57/9	0.98/3	1.01/3	1.02/4	1.07/2	1.07/4	1.10/5	1.19/5
	0.63/11	0.59/14	0.40/8	0.63/16	0.35/2	0.61/12	0.62/12	0.63/12	0.67/17	0.66/13	0.68/13	0.74/14
M97800	0.85 (0.99)	1.53 (1.34)	2.05 (1.37)	1.35 (1.38)	2.37 (1.74)	1.35 (1.39)	1.12 (1.34)	1.01 (1.23)	0.83 (0.98)	0.88 (1.18)	0.90 (1.38)	0.91 (1.51)
	0.94/14	0.72/14	0.54/16	0.85/13	0.62/16	0.83/14	0.95/15	0.98/16	0.98/10	1.02/18	1.17/19	1.36/17
	1.05/6	0.80/6	0.60/8	0.95/4	0.69/9	0.92/6	1.06/6	1.10/7	1.09/5	1.14/10	1.30/12	1.51/9
	0.65/8	0.50/8	0.37/4	0.59/11	0.42/3	0.57/8	0.66/7	0.68/6	0.68/16	0.71/6	0.80/5	0.92/5
M98800	1.26 (1.43)	1.53 (1.46)	2.45 (1.48)	1.49 (1.52)	2.90 (2.21)	1.47 (1.46)	1.41 (1.49)	1.35 (1.42)	1.20 (1.37)	1.18 (1.41)	1.19 (1.43)	1.18 (1.52)
	0.93/13	0.83/12	0.49/16	0.90/10	0.61/16	0.87/12	0.91/12	0.92/13	0.97/11	0.97/13	1.00/14	1.11/14
	1.03/4	0.92/4	0.55/9	1.00/2	0.67/9	0.97/2	1.01/2	1.03/3	1.08/2	1.08/5	1.12/6	1.23/5
	0.64/11	0.57/12	0.34/3	0.62/16	0.41/3	0.60/13	0.63/14	0.64/12	0.67/16	0.67/11	0.69/11	0.76/12
O64210	1.03 (1.11)	1.34 (1.25)	1.53 (1.22)	1.26 (1.22)	1.63 (1.35)	1.27 (1.21)	1.16 (1.24)	1.12 (1.25)	1.00 (1.13)	1.05 (1.26)	1.09 (1.31)	1.12 (1.36)
	0.92/13	0.75/15	0.63/16	0.85/14	0.67/17	0.82/15	0.90/14	0.93/13	0.97/11	0.95/16	0.98/17	1.03/15
	1.03/4	0.84/6	0.70/8	0.94/3	0.75/8	0.92/4	1.01/3	1.04/3	1.08/3	1.06/7	1.10/7	1.15/3
	0.64/12	0.52/10	0.44/6	0.58/14	0.46/6	0.57/12	0.63/14	0.64/15	0.67/17	0.66/10	0.68/10	0.71/13
O64530	0.91 (0.92)	1.27 (1.14)	1.56 (1.14)	1.12 (1.13)	1.67 (1.41)	1.13 (1.13)	0.95 (1.08)	0.92 (0.99)	0.91 (0.94)	0.93 (1.09)	0.95 (1.20)	0.94 (1.24)
	0.90/11	0.72/15	0.60/17	0.84/14	0.67/18	0.81/15	0.91/14	0.91/11	0.93/8	0.93/13	1.00/16	1.10/16
	1.00/2	0.80/7	0.66/9	0.94/5	0.75/9	0.90/7	1.02/6	1.02/4	1.04/6	1.04/6	1.12/8	1.23/6
	0.62/15	0.50/8	0.41/5	0.58/11	0.46/6	0.56/8	0.63/11	0.63/14	0.64/21	0.65/12	0.69/10	0.76/11
O64700	1.03 (1.04)	1.18 (1.09)	1.55 (1.12)	1.10 (1.09)	1.70 (1.41)	1.10 (1.06)	1.08 (1.03)	1.07 (1.10)	1.01 (1.02)	1.01 (1.05)	1.01 (1.12)	1.03 (1.22)
	0.91/12	0.76/14	0.59/17	0.87/12	0.66/18	0.85/12	0.89/11	0.91/11	0.94/10	0.92/13	0.95/13	1.00/12
	1.01/1	0.85/5	0.65/9	0.97/3	0.74/9	0.95/3	0.99/3	1.01/3	1.05/4	1.02/3	1.06/4	1.11/4
	0.62/16	0.53/10	0.41/4	0.60/15	0.46/6	0.58/14	0.62/18	0.63/18	0.65/20	0.63/14	0.66/14	0.69/15

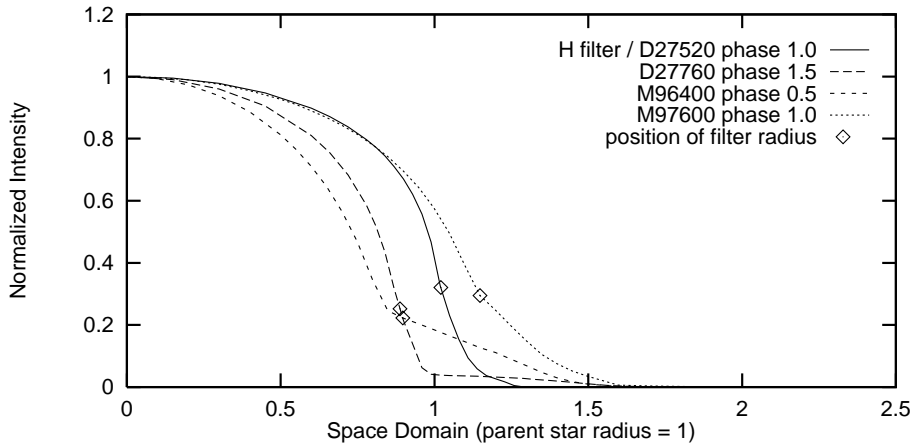


Fig. 4. Center-to-limb variation for the Mira models: models D and M in the H filter (Fig. 4), model O in the H filter (Fig. 5), model D in the 700 nm and 710 nm filters (Fig. 6; 700(D27520) ~ 700(D28760) omitted), model D at phase 1.0 in the 700 nm, 710 nm and 750 nm filters (Fig. 7), and model O in the 700 nm and 710 nm filters (Fig. 8; 710(O64700) ~ 710(O64530) omitted). The abscissa are in units of the parent star radii in Fig. 4 are different for the two models (D: 236 R_{\odot} ; M: 260 R_{\odot}). The diamonds give the positions of the filter radii R_{fil} after Scholz & Takeda (1987).

for the majority of Mira model-filter combinations, but it is also obvious that in many cases Gauss fits are substantially better and sometimes indeed perfect whereas just a handful of fair UD fits occur. Unfortunately, there is no rule of thumb to tell whether a FDD or a Gauss fit should be preferred for a spe-

cific model-filter pair. Continuum limb-darkening tends to be more FDD-like, and limb-darkening in strong TiO bands tends to be more Gauss-like, but there are numerous exceptions from this rule. Since most CLV shapes can be impressively well approximated by the one-parameter representation $I_{\lambda}(\mu) = \mu^{\alpha}$

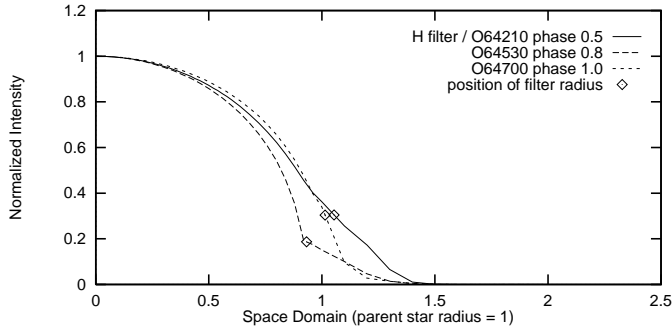


Fig. 5. See caption of Fig. 4

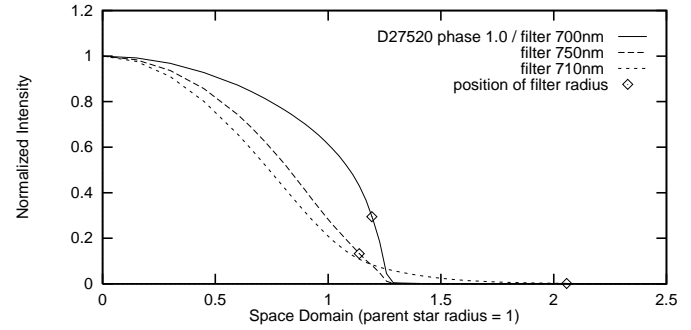


Fig. 7. See caption of Fig. 4

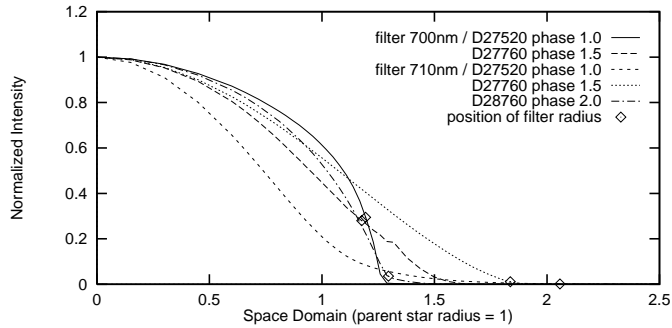


Fig. 6. See caption of Fig. 4

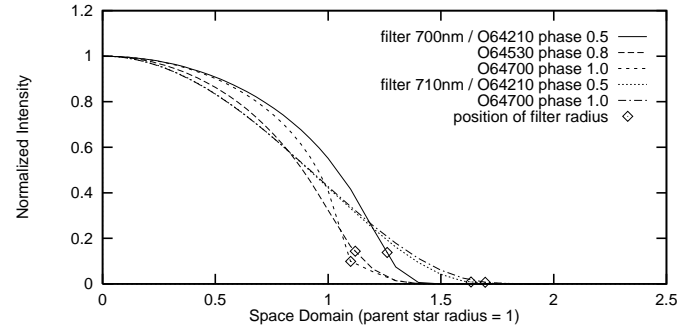


Fig. 8. See caption of Fig. 4

recently proposed by Hestroffer (1997), including the UD ($\alpha = 0$), the FDD ($\alpha = 1$) and Gauss-type disks (large α), we shall also consider this approximation in sample figures given below.

Figs. 4 and 5 show the continuum pulsation of three model series in terms of the CLV in the infrared H filter. Although infrared continuum limb-darkening is rather "simple" compared to complex molecular band CLV curves and is well approximated by a fully darkened disk in most models, differences of CLV shapes like those plotted in the two figures have to be taken into account if the star's "true pulsation", i.e. 10 to 20% phase changes of the position of the continuum forming layers, is to be measured (e.g. Burns et al. 1998). We also see from Table 4a/4b that different continuum radii may readily deviate from each other by a few percent owing to the wavelength-dependence of the Planck function creating the CLV, to slightly wavelength-dependent continuous absorption and to molecular band contamination. For instance, the continuum radii of the P series models are smaller at near-minimum phases than at near-maximum phases whereas substantial contamination shows up in the 0.82 and 0.92 near-continuum filters at the very low near-minimum temperatures and makes the star appear larger. Burns et al. (1998) measured at 0.83 and 0.94 μm a larger near-continuum radius of R Leo near its minimum, and it is not clear without detailed analysis whether this finding contradicts our model series (minimum $<$ or \sim maximum true-continuum radius), or is mimicked by contamination (compare 0.82/0.92 and 1.04 columns in Table 4a/4b), or is affected by using a UD fit. Note that cycle-to-cycle variations of continuum pulsation is generally small; the largest effects up to $\sim 10\%$ occur in our P series. It is also obvious from these considerations that effective

temperatures derived from different continuum radius measurements necessarily have an inherent scatter of the order of a few percent. We finally should point out for high-accuracy studies that the FDD brightness distribution was originally designed to approximate limb-darkening of a compact atmosphere where the zero-intensity "edge" of the disk marks the position of the radius. However, the position of an optical-depth type radius like R_{fil} on an extended-atmosphere CLV is slightly below the near-zero-intensity point even in the case of an almost perfect FDD shape.

The large extension of the Mira atmosphere compared to that of its static parent star may be judged from the monochromatic radii in the very strong TiO 0.71 μm band given in Table 4a/4b for Miras and in Table 2 of HS98 for non-Miras. Typical $R_{0.71}/R_{\text{continuum}}$ ratios range from 1.5 to 2.5 and may reach values >4 in the most extreme P models. Even the feature seen in the famous 0.75 μm spectral "window" may be formed at 1.5 or 2 times the distance of the real-continuum layers from the star's center. Table 4a/4b shows that molecular band radii do not only change strongly with phase but may also noticeably vary from cycle to cycle in agreement with recent observations of *o* Cet (Tuthill et al. 1995). The 0.71 μm entry for model P73600 was omitted in Table 4b because the CLV curve has not yet dropped to the near-zero level at the $5 R_p$ model "surface".

Fig. 6 shows the phase variation of limb-darkening in the moderate-TiO 0.70 and strong-TiO 0.71 filters for the D model series. Note the significant differences between two successive near-maximum phases whereas limb-darkening at the next near-minimum phase 2.5 not displayed here differs very little from that at phase 1.5. The 0.71 curve for model D27520 is one of the

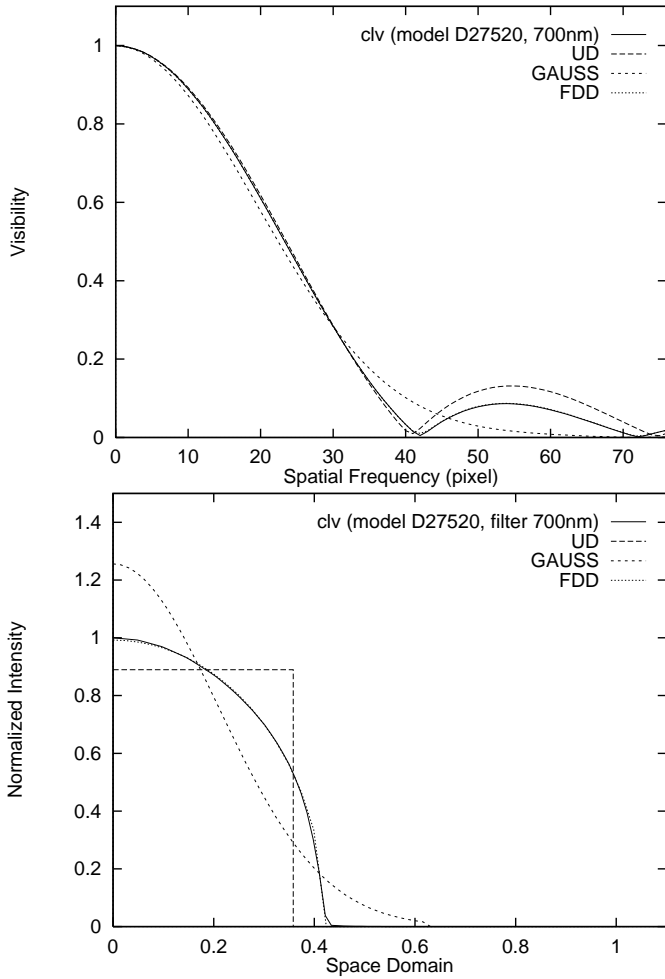


Fig. 9. Model D27520: (top) visibility plus the fitted visibilities of UD, FDD and Gaussian (visibility distances: 0.48%, 0.04% and 2.10%), (bottom) *true* clv plus clv of UD, FDD and Gaussian (with identical integrated intensities; clv distances: 11%, 1% and 16%). The artificial clv's UD, FDD and Gaussian displayed have not the same central intensity as the *true* clv, but they are all normalized to have the same integrated intensity value. Integral intensity normalization means the same visibility value at zeroth frequency for all these clv's. Integral intensity normalization is applied since integral visibility normalization (i.e. conventional central intensity normalization) requires the knowledge of the Fourier spectrum over the whole u - v plane, which observationally is not achievable.

few extreme (and hence particularly modelling-detail sensitive) examples of the above mentioned case of a narrow bright CLV core described by JBRS. The 0.71 disk appears narrower than the adjacent 0.70 disk in the light of the bright CLV portions and the unity optical-depth radius is positioned in the here excessively dim outermost CLV wing. Fig. 7 shows how the stellar disk size increases with increasing molecular band absorption from 0.75 to 0.70 μm but seems at first glance to shrink again as TiO absorption increases further at 0.71 μm . Note the pronounced Gauss-type shape of the 0.71 limb-darkening in D27520. Most striking examples occurring in the P model series are displayed in Fig. 2 (upper left panel: model P71800; upper right: P74200;

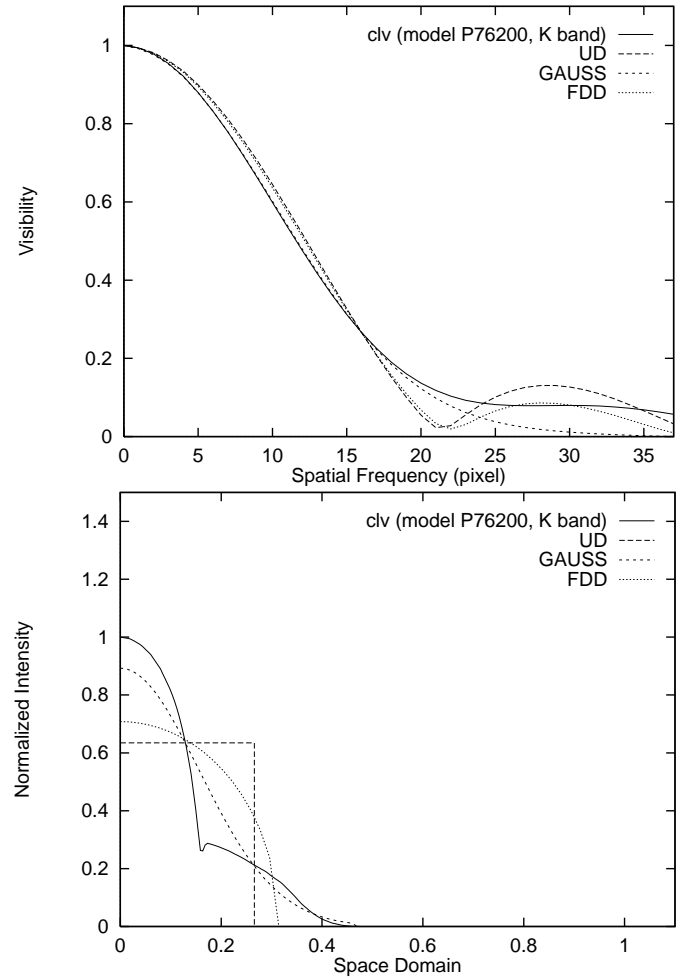


Fig. 10. Model P76200: (top) visibility plus the fitted visibilities of UD, FDD and Gaussian (visibility distances: 2.59%, 2.17% and 0.35%), (bottom) *true* clv plus clv of UD, FDD and Gaussian (with identical integrated intensities; clv distances: 21%, 15% and 9%).

lower right: P75800) of Scholz (1997) and discussed by JBRS. The problems of meaningful interpretation of TiO band observations even in the case of a fairly compact and un-spectacular model sequence may be judged from Fig. 8 giving 0.70 and 0.71 limb-darkening of our O model series. Tiny "spike"-like features occasionally seen in our model CLV curves are artifacts resulting from the relatively small number of model depth points and from simple stratification approximations near shock front discontinuities. As they hardly affect visibilities and the numbers in Table 4a/4b we did not re-run the model calculations with better numerical resolution in those cases.

Figs. 9 and 10 show visibilities predicted by the center-to-limb intensity variation of two sample model-filter combinations, plus those resulting from UD, FDD and Gauss brightness distributions fitted to the modelled ("true") CLV (see HS98 for computational details). Fig. 9 is an example of an excellent FDD fit to the limb-darkening curve, whereas Fig. 10 reveals severe problems of measuring without detailed CLV knowledge a radius near minimum phase even in the standard continuum

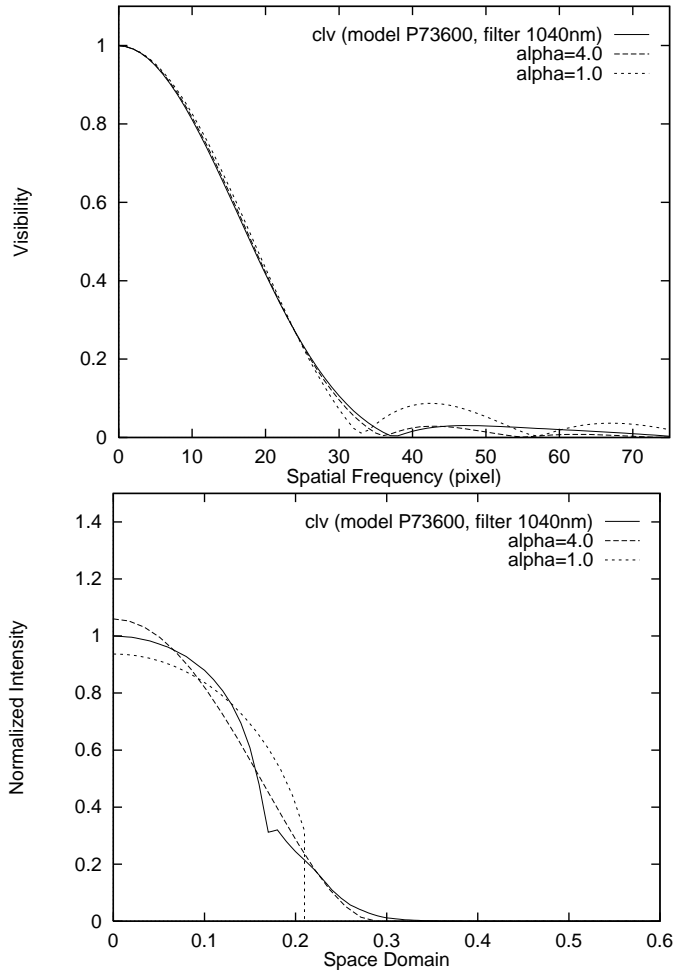


Fig. 11. Model P73600: (top) visibility plus the fitted visibilities of the best-fitting power law model ($\alpha=4.0$) and the FDD (visibility distances: 0.43% and 1.21%), (bottom) *true* clv plus clv of the power law model with $\alpha=4.0$ and FDD (with identical integrated intensities; clv distances: 3.3% and 8.1%).

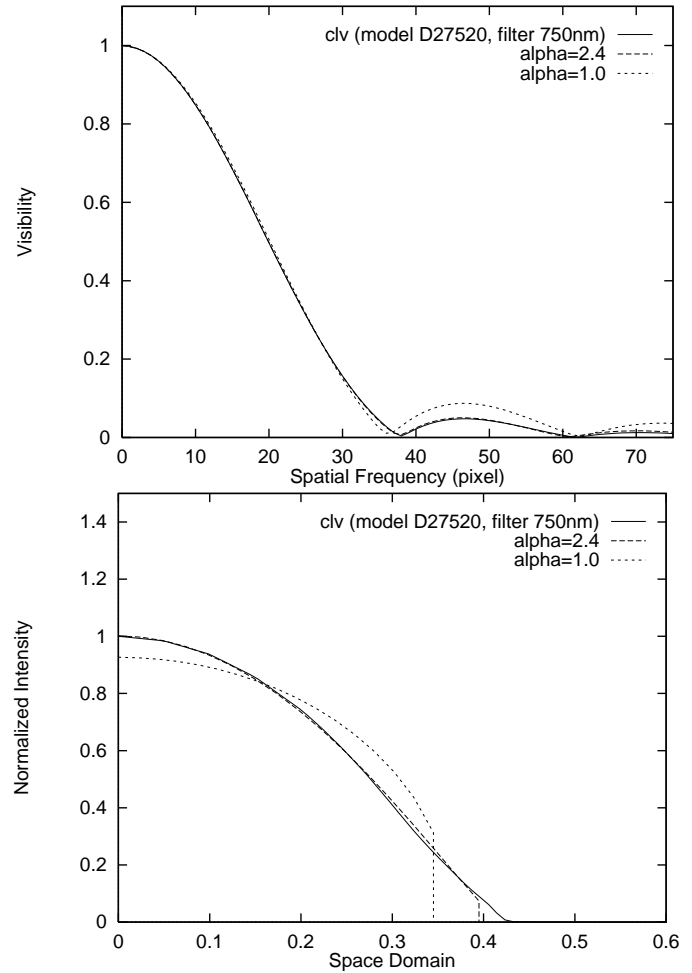


Fig. 12. Model D27520: (top) visibility plus the fitted visibilities of the best-fitting power law model ($\alpha=2.4$) and the FDD (visibility distances: 0.09% and 0.59%), (bottom) *true* clv plus clv of the power law model with $\alpha=2.4$ and FDD (with identical integrated intensities; clv distances: 0.6% and 5.3%).

K bandpass if the P model series were a good representation of the observed star.

Sample applications of Hestroffer's parametrization are shown in Figs. 11 and 12 for the $1.04\mu\text{m}$ filter in model P73600 and the $0.75\mu\text{m}$ filter in model D27520, respectively. Both CLV curves are just fairly represented by the $\alpha=1$ FDD limit (8% and 5% fitting accuracy in Table 4a/4b) whereas Hestroffer's power law approximation with $\alpha=2.4$ provides an excellent fit to the model-predicted intensity in Fig. 12 (0.6% fitting accuracy). In Fig. 11, a Hestroffer fit with $\alpha=4.0$ is somewhat better (3% fitting accuracy) than classical FDD limb-darkening but it is also obvious that such rather irregular CLV shapes are hard to describe satisfactorily in terms of a simple one-parameter approximation. (Fictitious discontinuities at the edge of Hestroffer curves in Figs. 11 and 12 result from our limited pixel resolution). As already stated in HS98, in terms of visibilities, however, observation of the side-maximum with an accuracy of the order of a few percent would be needed in order to tell apart a

power difference of $\Delta\alpha = 1$ (see top panels of Figs. 8 and 9 in HS98).

6. Discussion

We have seen two fundamental problems of measuring radii of M type Mira variables. First, comparison of the different series of the BSW96 and the new Mira models here presented show that relatively small changes of physical model parameters and computational modelling assumptions may result in drastic changes of atmospheric properties determining spectral characteristics and monochromatic limb-darkening. Furthermore, for a given star, these properties may depend sensitively upon the pulsation phase and even on the considered cycle. Whilst irregular spectral changes have been known for a long time (see, e.g., Joy 1954, and Fig. 9 in the classical review of Spinrad & Wing 1969), phase and cycle variations of the star's size became only recently accessible to observational instrumentation (e.g. Tuthill et al. 1995). Secondly, the huge geometric exten-

sion of the Mira atmosphere highlights the sometimes forgotten fact that the monochromatic center-to-limb intensity variation on the disk is the only geometry information the star sends to the observer, and that the choice of any specific distance from the disk's center defining a "radius" is an arbitrary (though often quite sensible) procedure.

Fortunately, various important features like the continuum CLV are only weakly to moderately model-dependent and can be rather safely related to a monochromatic radius. Other features do in principle require the knowledge of exact model parameters including phase for interpretation of interferometric or occultation observations but, on the other hand, may be used for model analysis owing to their sensitivity to model properties.

Observers find in Table 4 informations about typical CLV shapes and CLV model-dependence in selected filters, as well as informations about approximate corrections to be applied to classical UD, FDD and Gauss fits of visibilities. Limb-darkening in additional filters can be provided upon request when it is needed for data reduction of specific Mira observations.

Interpretation of "radius" measurements is most difficult for very cool and for very extended Mira atmospheres, in particular in the light of moderate to strong molecular bands. The information content of "impure" filters collecting light from both high (high-absorption) and deep (low-absorption) layers may be very low in Miras so that radius measurements with medium to broad bandpasses should be restricted to continuum observations. At very low effective temperatures, even continuum radius measurements pose problems resulting in noticeable inherent uncertainties of assigned T_{eff} values.

Acknowledgements. We thank W.J. Duschl for valuable comments. M.S. was supported by an ATC travel grant.

References

- Baschek B., Scholz M., Wehrse R. 1991, A&A 246, 374
 Bessell M.S., Brett J.M., Scholz M., Wood P.R. 1989a, A&AS 77,1 (erratum: 87, 621)
 Bessell M.S., Brett J.M., Scholz M., Wood P.R. 1989b, A&A 213, 209
 Bessell M.S., Brett J.M., Scholz M., Wood P.R. 1991, A&AS 89, 335
 Bessell M.S., Scholz M., Wood P.R. 1996, A&A 307, 481 (BSW96)
 Bogdanov M.B., Cherepashchuk A.M. 1991, SvA 35, 392
 Burns D., Baldwin J.E., Boysen A.C. et al. 1998, MNRAS 297, 462
 Claret A., Diaz-Cordoves J., Gimenez A. 1995, A&AS 114, 247
 Diaz-Cordoves J., Claret A., Gimenez A. 1995, A&AS 110, 329
 Di Giacomo A., Richichi A., Lisi F., Calamai G. 1991, A&A 249, 397
 Feast M.W., Robertson B.S.C., Catchpole R.M. et al. 1982, MNRAS 201, 439
 Haniff C.A., Scholz M., Tuthill P.G. 1995, MNRAS 276, 640
 Hestroffer D. 1997, A&A 327, 199
 Hinkle K.H., Scharlach W.W.G., Hall D.N.B. 1984, ApJS 56, 1
 Hofmann K.-H., Scholz M. 1998, A&A 335, 637 (HS98)
 Iglesias C.A., Rogers F.F. 1993, ApJ 412, 752
 Joy A.H. 1954, ApJS 1, 39
 Manduca A. 1979, A&AS 36, 411
 Manduca A., Bell R.A., Gustasson B. 1977, A&A 61, 809
 Scholz M. 1997, in: Bedding T.R., Booth A.J., Davis J. (eds.) Fundamental Stellar Properties: The Interaction between Observation and Theory, IAU Symp. 189, Kluwer, Dordrecht, p. 51
 Scholz M., Takeda Y. 1987, A&A 186, 200 (erratum: 196, 342)
 Spinrad H., Wing R.F. 1969, ARA&A 7, 249
 Tuthill P.G., Haniff C.A., Baldwin J.E., Feast M.W. 1994, MNRAS 266, 745
 Tuthill P.G., Haniff C.A., Baldwin J.E. 1995, MNRAS 277, 1541
 Van Belle G.T., Dyck H.M., Benson J.A., Lacasse M.G. 1996, AJ 112, 2147
 Van Hamme W. 1993, AJ 106, 2096
 Watanabe T., Kodaira K. 1979, PASJ 31, 61
 Wehrse R., Baschek B. 1998, Physics Reports, in press
 Wehrse R., Baschek B., Shaviv G. 1992, Rev. Mex. Astron. Astrof. 23, 247
 Weigelt G., Balega Y., Hofmann K.-H., Scholz M. 1996, A&A 316, L21
 Wilson R.W., Baldwin J.E., Buscher D.F., Warner P.J. 1992, MNRAS 257, 369
 Wood P.R. 1987, in: Cox A.N., Sparks W.M. (eds.) Stellar Pulsation, Lecture Notes in Physics 274, Springer, Berlin, p.250
 Wood P.R. 1990, in: Mennessier M.O., Omont A. (eds.) From Miras to Planetary Nebulae: Which Path of Stellar Evolution? Editions Frontieres, Gif sur Yvette, p.67
 Wood P.R. 1995, in: Stobie R.S., Whitelock P.A. (eds.) Astrophysical Applications of Stellar Pulsation, ASP Conf. Ser. 83, p.127
 Wood P.R. 1997, in: Bedding T.R., Booth A.J., Davis J. (eds.) Fundamental Stellar Properties: The Interaction between Observation and Theory, IAU Symp.189, Kluwer, Dordrecht, p.299
 Yaari A., Tuchman Y. 1995, in: Stobie R.S., Whitelock P.A. (eds.) Astrophysical Applications of Stellar Pulsation, ASP Conf. Ser. 83, p.139